PHYSICAL REVIEW D **103,** 063538 (2021)

Threshold for primordial black holes. II. A simple analytic prescription

Ilia Musco,[1,2,*] Valerio De Luca,[1,†] Gabriele Franciolini,[1,‡] and Antonio Riotto[1,3,§]

[1]*Département de Physique Théorique and CAP, Université de Genève,*
24 quai E. Ansermet, CH-1211 Geneva, Switzerland
[2]*Instituto Galego de Física de Altas Enerxías, Universidade de Santiago de Compostela,*
E-15782 Santiago de Compostela, Spain
[3]*INFN, Sezione di Roma, Piazzale Aldo Moro 2, 00185 Roma, Italy*

(Received 11 November 2020; accepted 18 February 2021; published 30 March 2021)

Primordial black holes could have been formed in the early universe from nonlinear cosmological perturbations reentering the cosmological horizon when the Universe was still radiation dominated. Starting from the shape of the power spectrum on superhorizon scales, we provide a simple prescription, based on the results of numerical simulations, to compute the threshold δ_c for primordial black hole formation. Our procedure takes into account both the nonlinearities between the Gaussian curvature perturbation and the density contrast and, for the first time in the literature, the nonlinear effects arising at horizon crossing, which increase the value of the threshold by about a factor two with respect to the one computed on superhorizon scales.

DOI: 10.1103/PhysRevD.103.063538

I. INTRODUCTION AND SUMMARY

It has been suggested that primordial black holes (PBHs) might form in the radiation dominated era of the early Universe by gravitational collapse of sufficiently large-amplitude cosmological perturbations [1–3] (see Refs. [4,5] for recent reviews), and that they can comprise a significant fraction of the dark matter in the universe, see Ref. [6] for a review of the current experimental constraints on the PBH abundance. This idea has recently received renewed attention given the possibility that PBHs might have given rise to gravitational waves detected during the O1/O2 and O3 observational runs [7–10] by the LIGO/Virgo Collaboration. This has motivated several studies on the primordial origin of these events [11–26]. In particular, the GWTC-2 catalog is found to be compatible with the primordial scenario [27]. Furthermore, a possible detection of a stochastic gravitational wave background by the NANOGrav collaboration [28] could be ascribed to PBHs [29–34].

Despite some pioneering numerical studies [35–37], it has only recently become possible to fully understand the mechanism of PBH formation with detailed spherically symmetric numerical simulations [38–41], showing that a cosmological perturbation collapses to a PBH if it has an amplitude δ greater than a certain threshold value δ_c. This quantity has been estimated initially using a simplified Jeans length argument in Newtonian gravity [42], obtaining $\delta_c \sim c_s^2$, where $c_s^2 = 1/3$ is the sound speed of the cosmological radiation fluid measured in units of the speed of light. More recently, this value has been refined generalising the Jeans length argument with the theory of general relativity, obtaining a value of $\delta_c \simeq 0.4$ for a radiation dominated Universe [43]. This analytical computation gives just a lower bound for the value of the threshold because it is not able to account for the nonlinear effects of pressure gradients, which require full numerical relativistic simulations. A recent detailed study has shown that there is a clear relation between the value of the threshold δ_c and the initial curvature (or energy density) profile, with $0.4 \leq \delta_c \leq 2/3$, where the shape is identified by a single parameter [44,45].

A consistent way to measure the amplitude of a perturbation is by using the relative mass excess inside the length scale of the perturbation, that for a consistent comparison between different shapes, should be measured at horizon crossing, when the length scale of the perturbation is equal to the cosmological horizon [44].

Numerical simulations have also shown that the mechanism of critical collapse discovered by Choptuik [46] is arising during the formation of PBHs, characterising the mass spectrum [47]. A crucial aspect to fully describe this mechanism was the implementation of an adaptive mesh refinement (AMR), which allows study of the critical behavior down to very small values of $(\delta - \delta_c)$ [48,49].

Numerical simulations modelling PBH formation start from initial conditions specified on superhorizon scales,

---

[*] ilia.musco@unige.ch
[†] valerio.deluca@unige.ch
[‡] gabriele.franciolini@unige.ch
[§] antonio.riotto@unige.ch

when the curvature perturbations describing adiabatic perturbations are time independent [50]. This allows expression of the initial conditions of the numerical simulations, such as the energy density and velocity field, only in terms of a time independent curvature profile [51,52], which can be derived, in the Gaussian approximation using peak theory [53], from the shape of the inflationary power spectrum of cosmological perturbations measured on superhorizon scales [54,55].

The relation between the shape of the peak of the curvature power spectrum and the initial conditions used in simulations for PBH formation has recently been investigated in both the Gaussian approximation, with the aim of obtaining a proper estimate of the cosmological abundance of PBHs [54–57], and including also corrections coming from nonlinearities [58–62] and non-Gaussianities [63–67]. On the other hand, numerical simulations have been used to reconstruct the shape of the peak of the inflationary power spectrum, understanding to which extent this is consistent with the observational constraint for PBH formation on different scales [68].

A. Prescription scheme

The aim of the present paper is to enable the interested reader to calculate the threshold for PBH formation, when the Universe is still radiation dominated, without the need for running numerical simulations. Although nonlinear cosmological density perturbations are described by a non-Gaussian random field, we provide a simple prescription to compute the threshold δ_c from the shape of the Gaussian inflationary power spectrum. The algorithm, divided into a few simple steps, accounts for both the nonlinearities associated with the relation between the Gaussian curvature perturbation and the density contrast as well as for those, so far neglected in the present literature, arising at horizon crossing. While a more refined description of the various steps will be found in the rest of the paper, we here provide the reader with an overview:

(1) The power spectrum of the curvature perturbation: take the primordial power spectrum $\mathcal{P}_\zeta$ of the Gaussian curvature perturbation and compute, on superhorizon scales, its convolution with the transfer function $T(k,\eta)$

$$P_\zeta(k,\eta) = \frac{2\pi^2}{k^3}\mathcal{P}_\zeta(k)T^2(k,\eta).$$

(2) The comoving length scale $\hat{r}_m$ of the perturbation is related to the characteristic scale k_* of the power spectrum P_ζ. Compute the value of $k_*\hat{r}_m$ by solving the following integral equation

$$\int dk k^2\left[(k^2\hat{r}_m^2-1)\frac{\sin(k\hat{r}_m)}{k\hat{r}_m}+\cos(k\hat{r}_m)\right]P_\zeta(k,\eta)=0.$$

(3) The shape parameter: compute the corresponding shape parameter α of the collapsing perturbation, including the correction from the nonlinear effects, by solving the following equation

$$F(\alpha)[1+F(\alpha)]\alpha=-\frac{1}{2}\left[1+\hat{r}_m\frac{\int dk k^4\cos(k\hat{r}_m)P_\zeta(k,\eta)}{\int dk k^3\sin(k\hat{r}_m)P_\zeta(k,\eta)}\right]$$

$$F(\alpha) = \sqrt{1-\frac{2}{5}e^{-1/\alpha}\frac{\alpha^{1-5/2\alpha}}{\Gamma(\frac{5}{2\alpha})-\Gamma(\frac{5}{2\alpha},\frac{1}{\alpha})}}.$$

(4) The threshold δ_c: compute the threshold as function of α, fitting the numerical simulations.

(a) At *superhorizon scales* making a linear extrapolation at horizon crossing ($aHr_m = 1$)

$$\delta_c \simeq \begin{cases} \alpha^{0.047}-0.50 & 0.1\lesssim\alpha\lesssim 7 \\ \alpha^{0.035}-0.475 & 7\lesssim\alpha\lesssim 13 \\ \alpha^{0.026}-0.45 & 13\lesssim\alpha\lesssim 30 \end{cases}.$$

(b) At *horizon crossing* taking into account also the non linear effects

$$\delta_c \simeq \begin{cases} \alpha^{0.125}-0.05 & 0.1\lesssim\alpha\lesssim 3 \\ \alpha^{0.06}+0.025 & 3\lesssim\alpha\lesssim 8 \\ 1.15 & \alpha\gtrsim 8 \end{cases}.$$

The difference between these two values of the threshold δ_c is discussed later in Sect. V.

Following the present Introduction, Sec. II reviews the mathematical formulation of the problem. In Sec. III we discuss the relation between the threshold δ_c and the shape of cosmological perturbation. In Sec. IV we show how to compute the typical value of the threshold δ_c as a function of the shape of the power spectrum, analyzing in detail some explicit examples. In Sec. V we compute, using numerical simulations, the amplitude of the threshold δ_c at horizon crossing, as a function of the shape parameter, discussing the difference when this is computed at horizon crossing or on superhorizon scales. Finally in Sec. VI conclusions are presented, making a summary of the results. Throughout we use $c = G = 1$.

II. INITIAL CONDITIONS FOR PBH FORMATION

A. Gradient expansion

PBHs form from the collapse of nonlinear cosmological perturbations after they reenter the cosmological horizon. Following the standard result for extreme peaks we assume spherical symmetry on superhorizon scales [53]. The local region of the Universe characterized by such perturbations is described by an asymptotic form of the metric, usually written as

$$\begin{aligned} \mathrm{d}s^2 &= -\mathrm{d}t^2 + a^2(t)\left[\frac{\mathrm{d}r^2}{1-K(r)r^2} + r^2\mathrm{d}\Omega^2\right] \\ &= -\mathrm{d}t^2 + a^2(t)e^{2\zeta(\hat{r})}[\mathrm{d}\hat{r}^2 + \hat{r}^2\mathrm{d}\Omega^2], \end{aligned} \tag{1}$$

where $a(t)$ is the scale factor, while $K(r)$ and $\zeta(\hat{r})$ are the conserved comoving curvature perturbations defined on a super-Hubble scale, converging to zero at infinity where the Universe is taken to be unperturbed and spatially flat. The equivalence between the radial and the angular parts gives

$$\begin{cases} r = \hat{r}e^{\zeta(\hat{r})}, \\ \frac{\mathrm{d}r}{\sqrt{1-K(r)r^2}} = e^{\zeta(\hat{r})}\mathrm{d}\hat{r}, \end{cases} \tag{2}$$

and the difference between the two Lagrangian coordinates r and $\hat{r}$ is related to the "spatial gauge" of the comoving coordinate, which is fixed by the form chosen to specify the curvature perturbation put into the metric, i.e., $K(r)$ or $\zeta(\hat{r})$. From a geometrical point of view the coordinate $\hat{r}$ considers the perturbed region as a local FRW separated universe, with the curvature perturbation $\zeta(\hat{r})$ modifying the local expansion, while the curvature profile $K(r)$ is defined with respect to the background FRW solution ($K = 0$). Combining the two expressions in (2) one gets

$$K(r)r^2 = -\hat{r}\zeta'(\hat{r})[2 + \hat{r}\zeta'(\hat{r})], \tag{3}$$

showing that $K(r)$ is more directly related to the spatial geometry of the spacetime, obtained as a quadratic correction in terms of $\hat{r}\zeta'(\hat{r})$.

On the superhorizon scales, where the curvature profile is time independent, we use the gradient expansion approach [39,51,69,70], based on expanding the time dependent variables such as energy density and velocity profile, as power series of a small parameter $\epsilon \ll 1$ up to the first nonzero order, where ϵ is conveniently identified with the ratio between the Hubble radius and the length scale of the perturbation. This approach reproduces the time evolution of linear perturbation theory but also allows having nonlinear curvature perturbations if the spacetime is sufficiently smooth on the scale of the perturbation (see [50]). This is equivalent to saying that pressure gradients are small when $\epsilon \ll 1$ and are not then playing an important role in the evolution of the perturbation.

In this approximation, the energy density profile can be written as [44,52]

$$\begin{aligned} \frac{\delta\rho}{\rho_b} \equiv \frac{\rho(r,t)-\rho_b(t)}{\rho_b(t)} &= \frac{1}{a^2H^2}\frac{3(1+w)}{5+3w}\frac{[K(r)r^3]'}{3r^2} \\ &= -\frac{1}{a^2H^2}\frac{4(1+w)}{5+3w}e^{-5\zeta(\hat{r})/2}\nabla^2 e^{\zeta(\hat{r})/2}, \end{aligned} \tag{4}$$

where $H(t) = \dot{a}(t)/a(t)$ is the Hubble parameter, ρ_b is the mean background energy density and $K'(r)$ denotes differentiation with respect to r while $\zeta'(\hat{r})$ and $\nabla^2\zeta(\hat{r})$ denote differentiation with respect to $\hat{r}$. The parameter w is the coefficient of the equation of state $p = w\rho$ relating the total (isotropic) pressure p to the total energy density ρ. From now on we are going to consider just the standard scenario for PBH formation assuming a radiation dominated Universe with $w = 1/3$.

B. The compaction function

The criterion to distinguish whether a cosmological perturbation is able to form a PBH depends on the amplitude measured at the peak of the compaction function [39,44] defined as

$$\mathcal{C} \equiv 2\frac{\delta M(r,t)}{R(r,t)}, \tag{5}$$

where $R(r,t)$ is the areal radius and $\delta M(r,t)$ is the difference between the Misner-Sharp mass within a sphere of radius $R(r,t)$, and the background mass $M_b(r,t) = 4\pi\rho_b(r,t)R^3(r,t)/3$ within the same areal radius but calculated with respect to a spatially flat FRW metric. In the superhorizon regime (i.e., $\epsilon \ll 1$) the compaction function is time independent, and is simply related to the curvature profile by

$$\mathcal{C} = \frac{2}{3}K(r)r^2 = -\frac{2}{3}\hat{r}\zeta'(\hat{r})[2 + \hat{r}\zeta'(\hat{r})]. \tag{6}$$

As shown in [44], the comoving length scale of the perturbation is the distance from $r = r_m$, where the compaction function reaches its maximum (i.e., $\mathcal{C}'(r_m) = 0$), which gives

$$K(r_m) + \frac{r_m}{2}K'(r_m) = 0, \tag{7}$$

or

$$\zeta'(\hat{r}_m) + \hat{r}_m\zeta''(\hat{r}_m) = 0. \tag{8}$$

Given the curvature profile, the parameter ϵ of the gradient expansion is defined as

$$\epsilon \equiv \frac{R_H(t)}{R_b(r_m,t)} = \frac{1}{aHr_m} = \frac{1}{aH\hat{r}_m e^{\zeta(\hat{r}_m)}}, \tag{9}$$

where $R_H = 1/H$ is the cosmological horizon and $R_b(r,t) = a(t)r$ is the background component of the areal radius. With these definitions, the expression written in Eq. (4) is valid for $\epsilon \ll 1$.

C. The perturbation amplitude and the threshold

We are now able to define consistently the perturbation amplitude as being the mass excess of the energy density within the scale r_m, measured at the cosmological horizon crossing time t_H, defined when $\epsilon = 1$ ($aHr_m = 1$). Although in this regime the gradient expansion approximation is not very accurate, and the horizon crossing defined in this way is only a linear extrapolation, this provides a well defined criterion to measure consistently the amplitude of different perturbations, understanding how the threshold is varying because of the different initial curvature profiles (see [44] for more details). Later in Sec. V we are going to extend the present discussion to include the nonlinear effect on the threshold when the cosmological horizon crossing is fully computed with numerical simulations.

The amplitude of the perturbation measured at t_H, which we refer to as $\delta_m \equiv \delta(r_m, t_H)$, is given by the excess of mass averaged over a spherical volume of radius R_m, defined as

$$\delta_m = \frac{4\pi}{V_{R_m}} \int_0^{R_m} \frac{\delta\rho}{\rho_b} R^2 \mathrm{d}R = \frac{3}{r_m^3} \int_0^{r_m} \frac{\delta\rho}{\rho_b} r^2 \mathrm{d}r, \tag{10}$$

where $V_{R_m} = 4\pi R_m^3/3$. The second equality is obtained by neglecting the higher order terms in ϵ, approximating $R_m \simeq a(t) r_m$, which allows to simply integrate over the comoving volume of radius r_m. Inserting the expression for $\delta\rho/\rho_b$ given by (4) into (10), one obtains $\delta_m = \mathcal{C}(r_m)$ and a simple calculation seen in [44] gives the fundamental relation

$$\delta_m = 3 \frac{\delta\rho}{\rho_b}(r_m, t_H). \tag{11}$$

PBHs form when the perturbation amplitude $\delta_m > \delta_c$, where the value of the threshold δ_c depends on the shape of the energy density profile, with $2/5 \leq \delta_c \leq 2/3$, as shown in [44]. Defining the quantity $\Phi \equiv -\hat{r}\zeta'(\hat{r})$ we can write δ_m as

$$\delta_m = \frac{4}{3} \Phi_m \left(1 - \frac{1}{2}\Phi_m\right) \tag{12}$$

where $\Phi_m = \Phi(\hat{r}_m)$, and the corresponding threshold for Φ is such that $0.37 \lesssim \Phi_c \leq 1$.

This shows that there are two different values of Φ_m corresponding to the same value of δ_m, with a maximum value of $\delta_m = 2/3$ for $\Phi_m = 1$. This degeneracy in the amplitude of the perturbation measured with δ_m is related to the difference between cosmological perturbations of Type I and Type II that have been carefully analyzed in [71]. Here we review this analysis in the context of PBHs formation.

The quantity Φ_m measures the perturbation amplitude in terms of the local curvature, uniquely defined, while the quantity δ_m is related to the global geometry, related to the compactness of the region or radius r_m, which has a degeneracy: there are two possible geometrical configurations of the spacetime with the same compactness as shown in Fig. 3 of [71]. When $\Phi > 1$ the spatial geometry of the spacetime starts to close on itself, up to $\Phi = 2$ corresponding to the *separate universe* limit.

Computing the first and second derivatives of $\mathcal{C}$ in terms of Φ gives

$$\mathcal{C}'(\hat{r}) = \frac{4}{3}\Phi'(\hat{r})(1 - \Phi(\hat{r})), \tag{13}$$

$$\mathcal{C}''(\hat{r}) = \frac{4}{3}[\Phi''(\hat{r})(1 - \Phi(\hat{r})) - (\Phi'(\hat{r}))^2]. \tag{14}$$

For a positive peak of the density contrast $\delta\rho/\rho_b$ we have $\mathcal{C}'(\hat{r}_m) = 0$ and $\mathcal{C}''(\hat{r}_m) < 0$, and one can distinguish between PBHs of Type I and Type II from the sign of Φ''_m.

(i) PBHs of Type I: $\delta_c < \delta_m \leq 2/3$ and $\Phi_c < \Phi_m \leq 1$.
In this case δ_m is increasing for larger values of Φ_m and $\mathcal{C}'(\hat{r}_m) = 0$ implies that $\Phi'_m = 0$, corresponding to the condition for $\hat{r}_m$ given in (8). When $\Phi_m \leq 1$ we have $\mathcal{C}''(\hat{r}_m) < 0$ corresponding to $\Phi''_m < 0$. In the limiting case of $\Phi_m = 1$ we have that both Φ''_m and $\mathcal{C}''(\hat{r}_m)$ are converging toward $-\infty$ (see after (23) for more explanations).

(ii) PBHs of Type II: $2/3 > \delta_m \geq 0$ and $1 < \Phi_m \leq 2$.
In this case δ_m is decreasing for larger values of Φ_m, and as before $\mathcal{C}'(\hat{r}_m) = 0$ implies that $\Phi'_m = 0$ (see Eq. (8)). For $\Phi_m > 1$ we have $\mathcal{C}''(\hat{r}_m) < 0$ while $\Phi''_m > 0$, changing sign with respect to Type I solutions.

All of the possible values of the threshold are within the regime of PBHs of Type I, where the mass spectrum of PBHs has a behavior described by the scaling law of critical collapse [44]

$$M_{\mathrm{PBH}} = \mathcal{K}(\delta_m - \delta_c)^\gamma M_H, \tag{15}$$

with $\gamma \simeq 0.36$ for a radiation dominated fluid, where M_H indicates the mass of the cosmological horizon measured at time t_H and $\mathcal{K}$ is a coefficient depending on the particular profile of $\delta\rho/\rho_b$. Numerical simulations have shown that $1 \lesssim \mathcal{K} \lesssim 10$, and that (15) is valid with γ constant when $\delta_m - \delta_c \lesssim 10^{-2}$.

III. THE SHAPE PARAMETER

As seen in [44,45], the threshold for PBHs depends on the shape of the cosmological perturbation, characterized by the width of the peak of the compaction function, measured by a dimensionless parameter defined as

$$\alpha = -\frac{\mathcal{C}''(r_m) r_m^2}{4\mathcal{C}(r_m)}, \tag{16}$$

where the family of curvature profiles $K(r)$ given by

$$K(r) = \mathcal{A} \exp\left[-\frac{1}{\alpha}\left(\frac{r}{r_m}\right)^{2\alpha}\right] \tag{17}$$

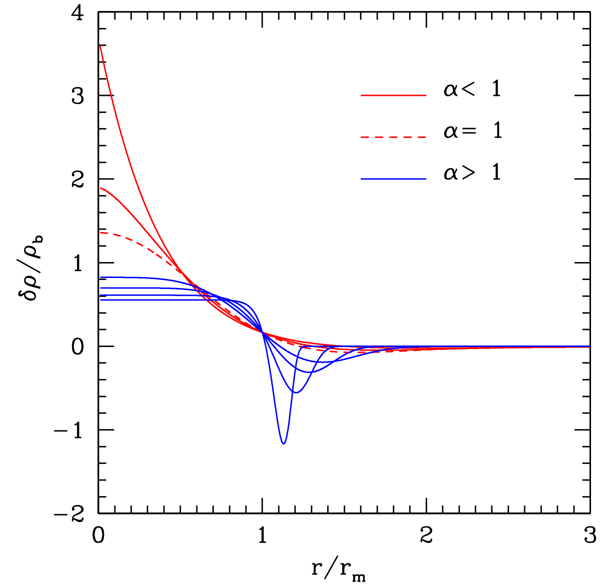

FIG. 1. This figure, taken from [44], shows the behavior of $\delta\rho/\rho_b$ given by (4) plotted against r/r_m when $aHr_m = 1$, for $\alpha = 0.5, 0.75, 1, 2, 3, 5, 10$. The profiles with $\alpha \leq 1$ are plotted with a red line (a dashed line for $\alpha = 1$) while blue lines are used for profiles with $\alpha > 1$.

identifies a basis of profiles which describes the main features of all of the possible shapes. In Fig. 1-taken from [44]-one can see the energy density profile $\delta\rho/\rho_b$ plotted against r/r_m, obtained by inserting (17) into (4) for different values of α, normalized at horizon crossing ($aHr_m = 1$). The shape of the energy density contrast becomes peaked for $\alpha < 1$ (red lines) corresponding to a broad profile of the compaction function, where the dashed line describes the typical Mexican-hat profile ($\alpha = 1$). On the contrary the shape of the compaction function $\mathcal{C}$ is more peaked for values of $\alpha > 1$ (blue lines), corresponding to broad profiles of the density contrast.

It is important to appreciate that when replacing (17) or any other K-profile into (16), the value of α is independent of the amplitude $\delta_m = \mathcal{C}(r_m)$ of the perturbation, related to the peak $\mathcal{A}$ of the curvature profile: this value is just an overall factor which cancels out in the ratio between the second derivatives and the value of the peak of the compaction function. The parameter α is therefore distinguishing between different shapes of the perturbation, independently of their amplitude.

As shown in [45], the average value of $\mathcal{C}(r)$ integrated over a volume of comoving radius r_m, defined as

$$\bar{\mathcal{C}}(r_m) = \frac{3}{r_m^3}\int_0^{r_m} \mathcal{C}(r) r^2 \mathrm{d}r, \tag{18}$$

has a nearly constant value when computed at the threshold for PBH formation, which is $\bar{\mathcal{C}}_c \simeq 2/5$. This allows derivation of an analytic expression to compute the threshold δ_c as a function of the shape parameter α, up to a few percent precision [45]

$$\delta_c \simeq \frac{4}{15} e^{-1/\alpha} \frac{\alpha^{1-5/2\alpha}}{\Gamma(\frac{5}{2\alpha}) - \Gamma(\frac{5}{2\alpha}, \frac{1}{\alpha})}, \tag{19}$$

where Γ identifies the special Gamma-functions. This is consistent with the analysis made in [44] where it was shown that the effects of additional parameters modifying the simple basis given by (17) are negligible.

The corresponding peak amplitude $\delta\rho_0/\rho_b$, corresponding to the overdensity amplitude evaluated at the centre of symmetry, is related to the value of δ_m by $\delta\rho_0/\rho_b = e^{1/\alpha}\delta_m$, which combined with (19) gives

$$\left(\frac{\delta\rho_0}{\rho_b}\right)_c \simeq \frac{4}{15} \frac{\alpha^{1-5/2\alpha}}{\Gamma(\frac{5}{2\alpha}) - \Gamma(\frac{5}{2\alpha}, \frac{1}{\alpha})}. \tag{20}$$

The shape parameter α describes the main features of the profile in the region $0 < r \lesssim r_m$ where PBHs form, while any other additional parameters describe only secondary modification of the tail, $r \gtrsim r_m$, giving only a few percent deviation of the value of δ_c with respect to the one obtained with (17).

The shape is not correlated with the amplitude of the perturbation when the shape is measured in the r-gauge of the comoving coordinate, while a correlation arises when measured in the $\hat{r}$-gauge. Using the coordinate transformation of (2) one obtains that

$$\mathcal{C}''(r_m) = \frac{1}{e^{2\zeta(\hat{r}_m)}[1 + \hat{r}_m\zeta(\hat{r}_m)]^2}\mathcal{C}''(\hat{r}_m), \tag{21}$$

where the additional term proportional to $\mathcal{C}'(\hat{r})$ is equal to zero when calculated at $\hat{r}_m$ because of (8). As stated in the introduction, the prime denotes spatial derivative with respect to the variable written explicitly in the argument of the function. The shape parameter can therefore be written as

$$\alpha = -\frac{\mathcal{C}''(\hat{r}_m)\hat{r}_m^2}{4\mathcal{C}(\hat{r}_m)[1 - \frac{3}{2}\mathcal{C}(\hat{r}_m)]}, \tag{22}$$

showing that the peak of the compaction function does not cancel out with the peak of the second derivative, when computed with respect to $\hat{r}$ instead of r.

Using (12), this can be written as

$$\alpha = -\frac{\Phi_m'' \hat{r}_m^2}{4\Phi_m(1 - \frac{1}{2}\Phi_m)(1 - \Phi_m)}, \tag{23}$$

showing that in general, when varying the amplitude of the perturbation, the values of Φ_m'' and Φ_m are not independent, but correlated, changing according to the given value of α. It is interesting to note that both Type I ($\Phi_m'' \leq 0, \Phi_m \leq 1$) and Type II ($\Phi_m'' > 0, \Phi_m > 1$) perturbations have $\alpha > 0$, consistently with (16).

In general there is a correlation between the shape of Φ and the amplitude of the peak Φ_m. In the upper limit of the Type I solution, when $\Phi_m \to 1$, one finds $\alpha \to \infty$ which implies from (14) that $\Phi_m'' \to -\infty$ because $\mathcal{C}''(r_m) < 0$ for any positive peak of the compaction function. From the geometrical point of view the shape of the compaction function is forced to be a Dirac delta (a top hat in the energy contrast) when $\Phi_m = 1$, corresponding to the threshold for PBH formation when $\alpha \to \infty$.

To give an explicit example of the correlation between the amplitude and the shape of $\zeta(\hat{r})$ we can consider the profile used in [59]

$$\zeta(\hat{r}) = \mathcal{B} \exp\left[-\left(\frac{\hat{r}}{\hat{r}_m}\right)^{2\beta}\right], \tag{24}$$

that inserted into the (23) gives

$$\alpha = \frac{\beta^2}{(1-\beta\zeta(\hat{r}_m))(1-2\beta\zeta(\hat{r}_m))}. \tag{25}$$

In the linear approximation $\mathcal{B} \ll 1 \Rightarrow \beta\zeta(\hat{r}_m) \ll 1$, which gives $\alpha \simeq \beta^2$, showing that for a given value of α, the corresponding value of β is fixed and there is no correlation between the shape and the amplitude, while when we are considering a perturbation amplitude of the order of the threshold δ_c, one has $\mathcal{B} \sim 1$ (corresponding to $\mathcal{A} r_m^2 \sim 1$) and the correlation is not negligible. For example, when $\alpha = 1$ one has a typical Mexican-hat shape and a value of the threshold $\delta_c \simeq 0.5$, while for a value of $\beta = 1$ corresponding to a Mexican-hat shape in the linear approximation, the value of the threshold is $\delta_c \simeq 0.55$, as seen in [59].

A. The nonlinear component of the shape

If ζ is a Gaussian random variable, also Φ_m, and $\Phi_m'' \hat{r}_m^2$ obey Gaussian statistics. In such case we can write the shape parameter given by (22) as

$$\alpha = \frac{\alpha_G}{(1-\frac{1}{2}\Phi_m)(1-\Phi_m)}, \tag{26}$$

where

$$\alpha_G = -\frac{\Phi_m'' \hat{r}_m^2}{4\Phi_m} \tag{27}$$

is the Gaussian shape parameter obtained in the linear approximation ($\Phi_m \ll 1$), independent of the amplitude of Φ_m since $\Phi_m'' \propto \Phi_m$ as, for instance, one can understand by computing the average of Φ_m'' given a realisation of Φ_m using conditional probability.

The value of Φ_m introduces a correction, which is negligible in the linear regime when $\Phi_m \ll 1$. On the other hand, when the value of Φ_m is nonlinear, the term $(1-\Phi_m)(1-\Phi_m/2)$ gives a non-negligible modification of the value of α with respect α_G. In general α depends on the statistics of Φ_m'' and the amplitude Φ_m.

Considering Type I solutions one can write Φ_m as a function of δ_c using (12), which gives

$$\Phi_m = 1 - \sqrt{1 - \frac{3}{2}\delta_c}, \tag{28}$$

and then inserting this equation combined with (19) into (26) one obtains

$$F(\alpha)[1+F(\alpha)]\alpha = 2\alpha_G, \tag{29}$$

where

$$F(\alpha) = \sqrt{1 - \frac{2}{5} e^{-1/\alpha} \frac{\alpha^{1-5/2\alpha}}{\Gamma(\frac{5}{2\alpha}) - \Gamma(\frac{5}{2\alpha}, \frac{1}{\alpha})}}. \tag{30}$$

The numerical solution of Eq. (29) gives a value of α as a function of α_G. By inserting this into (19), one can compute

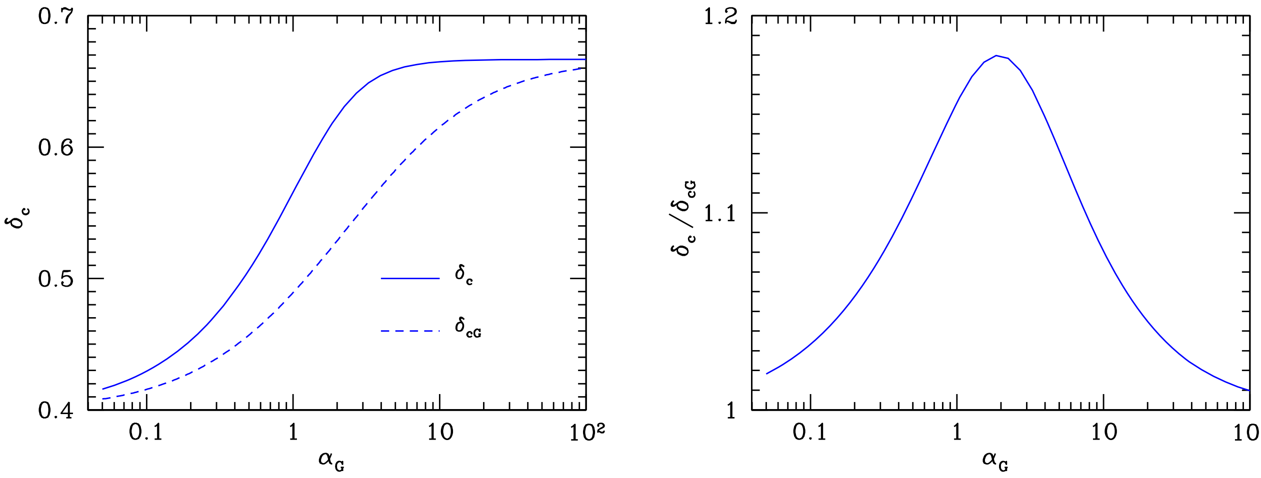

FIG. 2. The left panel of this figure shows the behavior of δ_c and $\delta_{cG} = \delta_c(\alpha_G)$ plotted as a function of the Gaussian shape parameter α_G. The right panel shows the ratio of these two quantities: the difference is due to the nonlinear effects coming from the solution of (29).

the value of δ_c as a function of α_G, which is plotted in the left panel of Fig. 2 using a solid line. This is compared with the analytic behavior of $\delta_{cG} = \delta_c(\alpha_G)$ plotted with the dashed line.

The right panel of Fig. 2 shows the ratio of these two quantities as function of α_G, and one can appreciate the correction of δ_c due to the modification of the shape with respect to the one obtained in the Gaussian approximation, because of the nonlinear effects. Because at the boundaries $F(0) \to 1$ $(F(\infty) = 1)$, there is no modification with respect to the Gaussian case and $\delta_c = \delta_{cG}$ in the limits $\alpha \to 0$ $(\alpha \to \infty)$.

IV. THE AVERAGE VALUE OF δ_c

The aim of this section is to describe how to calculate the average value of the shape parameter α, identifying which is the typical perturbation shape associated with a given cosmological power spectrum, which gives the corresponding averaged value of the threshold δ_c.

Assuming Gaussian statistics for the comoving curvature perturbation ζ, the first step is to compute the value of α_G from the power spectrum $P_\zeta(k,\eta)$ defined as

$$P_\zeta(k,\eta) = \frac{2\pi^2}{k^3}\mathcal{P}_\zeta(k)T^2(k,\eta), \tag{31}$$

computed at the proper time η when $\hat{r}_m \gg r_H$, where $r_H = 1/aH$ is the comoving Hubble radius. $\mathcal{P}_\zeta(k)$ is the dimensionless form of the power spectrum, and the linear transfer function $T(k,\eta)$, given by

$$T(k,\eta) = 3\frac{\sin(k\eta/\sqrt{3}) - (k\eta/\sqrt{3})\cos(k\eta/\sqrt{3})}{(k\eta/\sqrt{3})^3}, \tag{32}$$

has the effect of smoothing out the subhorizon modes, playing the role of the pressure gradients during the collapse. This smoothing should be done when $\hat{r}_m \simeq 10 r_H$ or larger, according to the gradient expansion approach used to specify the initial condition of the numerical simulations. This ensures that modes collapsing within the scale r_H does not affect the collapse on the larger scale $\hat{r}_m$. The details of how to apply the smoothing have been extensively discussed in [68], showing that using just the transfer function on superhorizon scales avoids the need of introducing a window function on the scale $\hat{r}_m$ of the perturbation, which introduces corrections in the calculation of the threshold that, however, are reduced when computing the PBH abundance if the same window function is adopted for evaluating the variance [72].

The radius $\hat{r}_m$ is obtained from condition (8), which can be expressed in terms of the power spectrum using Gaussian peak theory to write $\zeta(\hat{r})$

$$\zeta(\hat{r}) = \zeta_0 \int dk k^2 \frac{\sin(k\hat{r})}{k\hat{r}} P_\zeta(k,\eta), \tag{33}$$

and, applying $\Phi'(\hat{r}_m) = 0$, one finally gets

$$\int dk k^2 \left[(k^2\hat{r}_m^2 - 1)\frac{\sin(k\hat{r}_m)}{k\hat{r}_m} + \cos(k\hat{r}_m)\right] P_\zeta(k,\eta) = 0, \tag{34}$$

where this integral equation, in general, has to be solved numerically given the expression of P_ζ.

The Gaussian shape parameter can be computed from the average profile of $\zeta(\hat{r})$ shown in (33), which allows α_G to be written as

$$\alpha_G = \frac{1}{2} - \frac{\hat{r}_m^2}{4}\frac{\zeta'''(\hat{r}_m)}{\zeta'(\hat{r}_m)}, \tag{35}$$

where we have used the constraint relation $\Phi'(\hat{r}_m) = 0$, which gives

$$\hat{r}_m^2 \Phi''_m = \hat{r}_m[2\zeta'(\hat{r}_m) - \hat{r}_m^2\zeta'''(\hat{r}_m)]. \tag{36}$$

Inserting (33) into the expression for α_G, combined with (34) one obtains

$$\alpha_G = -\frac{1}{4}\left[1 + \hat{r}_m \frac{\int dk k^4 \cos(k\hat{r}_m) P_\zeta(k,\eta)}{\int dk k^3 \sin(k\hat{r}_m) P_\zeta(k,\eta)}\right], \tag{37}$$

showing that α_G, and the corresponding value of α computed using (29), are varying with the shape of the cosmological power spectrum. The same holds for the value of $\hat{r}_m$ given by the solution of (34). The values of α_G and α can then be used in (19) so as to calculate the corresponding values of δ_{cG} and δ_c, obtaining a direct relation between the threshold and the particular shape of the cosmological power spectrum P_ζ.

In the following we are going to apply this prescription to study the extent to which, given a particular form of the power spectrum, the amplitude of the threshold δ_c is varying.

A. Peaked power spectrum

The simplest cosmological power spectrum of the comoving curvature perturbation that can be considered is monochromatic, behaving like a Dirac-delta distribution, typically written as

$$\mathcal{P}_\zeta(k) = \mathcal{P}_0 k_* \delta_D(k - k_*). \tag{38}$$

Inserting this into (34) we get $k_*\hat{r}_m \simeq 2.74$, which gives $\delta_{c,G} \simeq 0.51$, a value of the threshold in the Gaussian approximation consistent with the one obtained in [54]. Solving equation (29), we can see the corresponding modification of δ_c due to the nonlinear effects, giving $\alpha \simeq 6.33$ corresponding to $\delta_c \simeq 0.59$.

It is interesting to note that this value of the threshold is consistent with the one found if the average profile of $\zeta(r)$ for a peaked power spectrum, characterized by the sync function, is inserted into (4) to specify the initial conditions for the numerical simulations [67]. This is consistent with the fact that using peak theory in ζ or in the density contrast $\delta\rho/\rho_b$ is equivalent when the power spectrum is very peaked, behaving like a Dirac delta [60].

B. Broad power spectrum

A class of models with a broad and flat power spectrum of the curvature perturbations of the form [73,74]

$$\mathcal{P}_\zeta(k) = \mathcal{P}_0 \Theta(k - k_{\mathrm{min}}) \Theta(k_{\mathrm{max}} - k), \qquad k_{\mathrm{max}} \gg k_{\mathrm{min}} \tag{39}$$

is another simple toy model, corresponding to the top hat shape of the primordial power spectrum, which is considered in [54]. In this case, from (34) we have $k_{\mathrm{max}} \hat{r}_m \simeq 4.49$, which gives $\alpha_G \simeq 0.9$ and $\delta_{c,G} \simeq 0.48$.

The values of $k_{\mathrm{max}} \hat{r}_m$ and $\delta_{c,G}$ obtained here are different from the values $k_{\mathrm{max}} \hat{r}_m \simeq 3.5$ and $\delta_{c,G} \simeq 0.51$ found in [54], because in that analysis peak theory was applied directly to the linearized density contrast $\delta\rho/\rho_b$ while here, instead, we are using peak theory to compute the average curvature perturbation ζ and account for the nonlinear relation with the compaction function. For this reason the integrals in peak theory for finding $\hat{r}_m$ and the shape profile $\zeta(\hat{r})$ are characterized by a higher power in k.

Solving Eq. (29) to include the nonlinear effects gives $\alpha \simeq 3.14$ corresponding to $\delta_c \simeq 0.56$.

C. Gaussian power spectrum

The gaussian shape of the curvature power spectrum given by

$$\mathcal{P}_\zeta(k) = \mathcal{P}_0 \exp\left[-(k - k_*)^2/2\sigma^2\right], \tag{40}$$

is characterized by the central reference scale k_* and width σ. Solving (34), the relation between the length scale $\hat{r}_m$ of the perturbation and the scale k_* is shown in the left panel of Fig. 3. As one can appreciate, in the limit of the narrow case $\sigma \to 0$ the result converges to the one obtained for a monochromatic shape of the curvature power spectrum (studied previously in the peaked case), while for broader shapes the expected length scale of the overdensity multiplied by k_* is decreasing. This is a result of the fact that, for broader shapes, more modes are contributing to the collapse, resulting in a narrower curvature profile.

The behavior of the shape parameter α, which decreases as σ increases, reflects the fact that when multiple modes are participating in the collapse, the compaction function becomes flatter. As a consequence, the pressure gradients are reduced, facilitating the collapse, and the corresponding threshold for PBHs decreases for larger values of σ, as one can appreciate in the right panel of the same figure. As discussed in the previous section and shown in Fig. 2, as nonlinearities are taken into account, the critical threshold δ_c reaches larger values than tat for δ_{cG} computed in the Gaussian approximation.

D. Lognormal power spectrum

The lognormal power spectrum is expressed as

$$\mathcal{P}_\zeta(k) = \mathcal{P}_0 \exp\left[-\ln^2(k/k_*)/2\sigma^2\right], \tag{41}$$

characterized by a width σ and a central scale k_*. The relation between the length scale of the overdensity and the

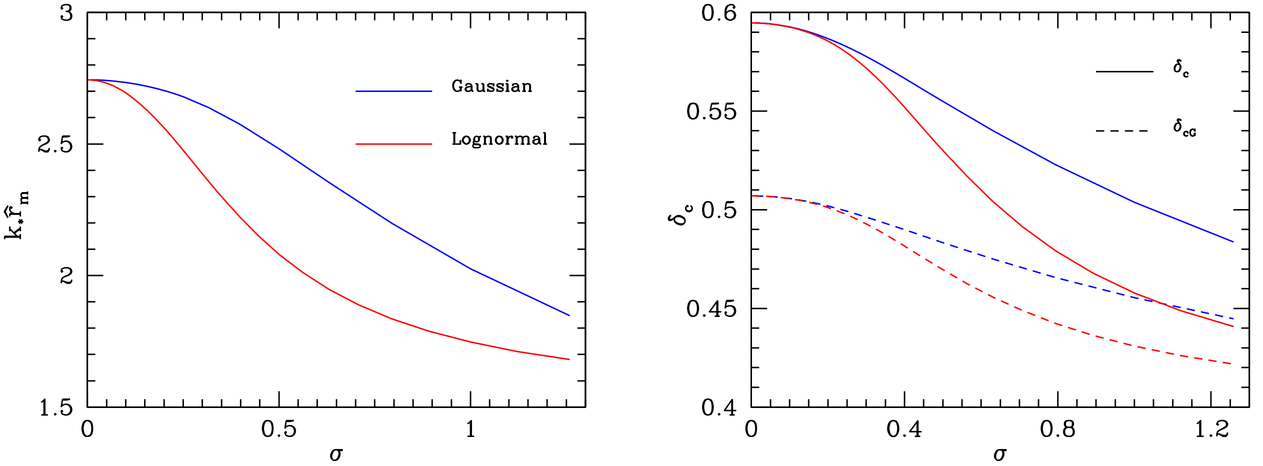

FIG. 3. Left: peak position of the compaction function $\hat{r}_m$ for both the case of a gaussian and lognormal shape of the power spectrum. Right: average threshold for collapse for both the $\delta_{cG}(\alpha_G)$ and its corresponding nonlinearly corrected δ_c in both cases. In the limit of $\sigma \to 0$, both spectra converge to the monochromatic case and the result is compatible with the Dirac delta example.

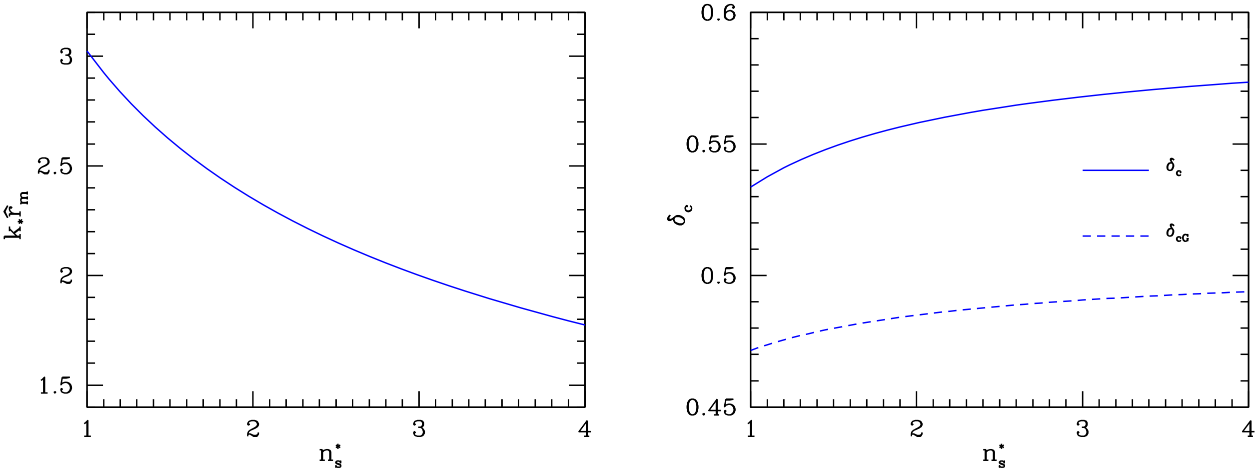

FIG. 4. The same as in Fig. 3, but for the cut-power-law power spectrum.

scale k_* is plotted in the left panel of Fig. 3, while the right panel is showing the average threshold for PBHs, showing the same qualitative behaviors found for the Gaussian power spectrum.

Because σ in this case identifies the width of the power spectrum in logarithmic space, larger values of σ allow for more modes to be part of the collapse. As a consequence, if compared to the Gaussian case, the trends for the relative change of $k_*\hat{r}_m$ and δ_c are amplified.

E. Cut-power-law power spectrum

The cut-power-law curvature power spectrum is given by

$$\mathcal{P}_\zeta(k) = \mathcal{P}_0\left(\frac{k}{k_*}\right)^{n_s^*}\exp\left[-(k/k_*)^2\right], \tag{42}$$

expressed in terms of a tilt n_s^* and with an exponential cutoff at the momentum scale k_*. The relation between the length scale of the overdensity and the scale k_* is shown in the left panel of Fig. 4, while the right panel of this figure is showing the behavior of the average threshold for PBHs.

As n_s^* increases, the spectrum becomes narrower, with a shift toward a higher value of the power spectrum peak which is identified by the maximum of the combined product of $k^{n_s^*}$ and the exponential cutoff. In agreement with the behavior seen in the previous examples, as the spectral tilt decreases, a larger number of modes participate in the collapse, resulting in a lower value of the threshold δ_c.

F. Summary

The analysis of this section of different power spectra shows that, when the shape is broader, the value of the threshold δ_c is lower because more modes are involved in the collapse. The maximum value we have found is $\delta_c \simeq 0.59$ when the power spectrum behave like a Dirac delta (corresponding to a single mode). The behavior for the lognormal power spectrum that one can extrapolate looking at the right panel of Fig. 3 indicates the possibility of getting closer to the lower boundary of 0.4 for very large values of σ. In conclusion the shapes of the power spectra we have considered here allows $0.4 \lesssim \delta_c \lesssim 0.6$, when the threshold is computed on superhorizon scales.

V. THE NONLINEAR HORIZON CROSSING

In this section we study the effects on the threshold when the cosmological horizon crossing is computed during the numerical evolution, measuring the amplitude δ_m of the perturbation when the length scale R_m is equal to the cosmological horizon radius R_H defined with respect to the perturbed medium. The numerical code used for the simulations is the same as used in previous works (see [44] and references therein for more details).

The threshold for PBHs has so far been computed at cosmological horizon crossing by making a linear extrapolation from the superhorizon regime, where the curvature is time independent, imposing $aHr_m = 1$ in Eq. (4), where the cosmological horizon $R_H = 1/H$ is defined with respect to the background. In this way one is extending the validity of the gradient expansion approximation up to $\epsilon = 1$, which is not very accurate. Although this represents a well-defined criterion for measuring the perturbation amplitude, and has been widely used in the literature to compute the threshold δ_c for PBHs, it does not give the correct amplitude of the perturbation at the "real" cosmological horizon crossing, because it is neglecting the nonlinear effects of the higher orders in the gradient expansion approach, which are taking into account that the curvature profile ζ starts to vary with time when $\epsilon \sim 1$.

In general the cosmological horizon is a marginally trapped surface within an expanding region, which in spherical symmetry is simply defined by the condition $R(r,t) = 2M(r,t)$, where $R(r,t)$ is the areal radius and $M(r,t)$ is the mass within a given sphere of radius $R(r,t)$, called the Misner-Sharp mass. This relation for a trapped surface is very general, assuming only spherical symmetry, and allows computation of the location of any apparent horizon: if we have an expanding medium, this is a cosmological horizon, while if the medium is collapsing then it is a black hole apparent horizon [75,76].

In simulations of PBH formation, because we are in a locally closed Universe, the rate of expansion of the cosmological horizon is less than that of the spatially flat background, and this gives rise to an additional growth of the amplitude of the perturbation before reaching the horizon crossing.

The left plot of Fig. 5 shows the critical energy density profile obtained with the curvature perturbation given by (17), with $\alpha = 1$ corresponding to a Mexican-hat shape, computed at the horizon crossing linearly extrapolated (blue line) and at the nonlinear horizon crossing obtained from the numerical simulations (red line). The second profile shows an additional growth of the amplitude, which is not negligible when the value of the energy density obtained with the linear extrapolation is nonlinear. Part of this extra growth is due to the longer time necessary to reach the nonlinear horizon crossing which can be seen explicitly in the right plot where $\epsilon(t_H)$ is plotted against the shape parameter α, with the dashed line fitting the numerical results given by the dots. We can appreciate that the value of $\epsilon(t_H)$ at the nonlinear horizon crossing, $1.3 \lesssim \epsilon(t_H) \lesssim 1.5$, is larger than one given by the linear horizon crossing ($aHr_m = 1$). In particular, for $\alpha = 1$ the nonlinear horizon crossing is obtained at $\epsilon(t_H) \simeq 1.46$, corresponding to an amplitude of the central peak calculated with (4) equal to $\delta\rho_0/\rho_b \simeq 1.98$, as compared with the value of $\delta\rho_0/\rho_b \simeq 1.35$ computed at the linear horizon crossing (blue line). The additional growth of the profile, with a peak value of the density contrast $\delta\rho_0/\rho_b \simeq 3.34$ obtained numerically at the nonlinear horizon crossing (red line), is explained by the higher orders in the gradient expansion which need to be taken into account when $\epsilon \sim 1$. This effect is genuinely nonlinear.

The delay of the horizon crossing due to the nonlinear effects gives an increase of the final mass of PBHs because of the corresponding increase of the cosmological horizon mass M_H: during the radiation dominated universe $M_H \sim \epsilon^2$ and from Fig. 5 one can appreciate the change of the horizon scale introducing a correction value about equal to 2 (i.e., $1.7 \div 2.2$) in the cosmological horizon mass.

In the left panel of Fig. 6 we are comparing the critical energy density profiles obtained from (17) for $\alpha = 0.15$, which gives a very sharp profile, almost like a Dirac-delta, while in the right panel we plot the critical profiles computed for $\alpha = 30$, which gives a very broad profile, very similar to a top-hat. As with the Mexican-hat shape, the profile in the right frame computed at the nonlinear horizon crossing is characterized by an extra growth of the peak: the numerical evolution gives $\delta\rho_0/\rho_b \simeq 1.46$ at $\epsilon(t_H) \simeq 1.31$ as compared with $\delta\rho_0/\rho_b \simeq 0.66$ obtained at $\epsilon = 1$ with the linear extrapolation. As in Fig. 5 for $\alpha = 1$, this difference is a result of the combination of the extra linear growth due to the larger value of ϵ and the nonlinear effects.

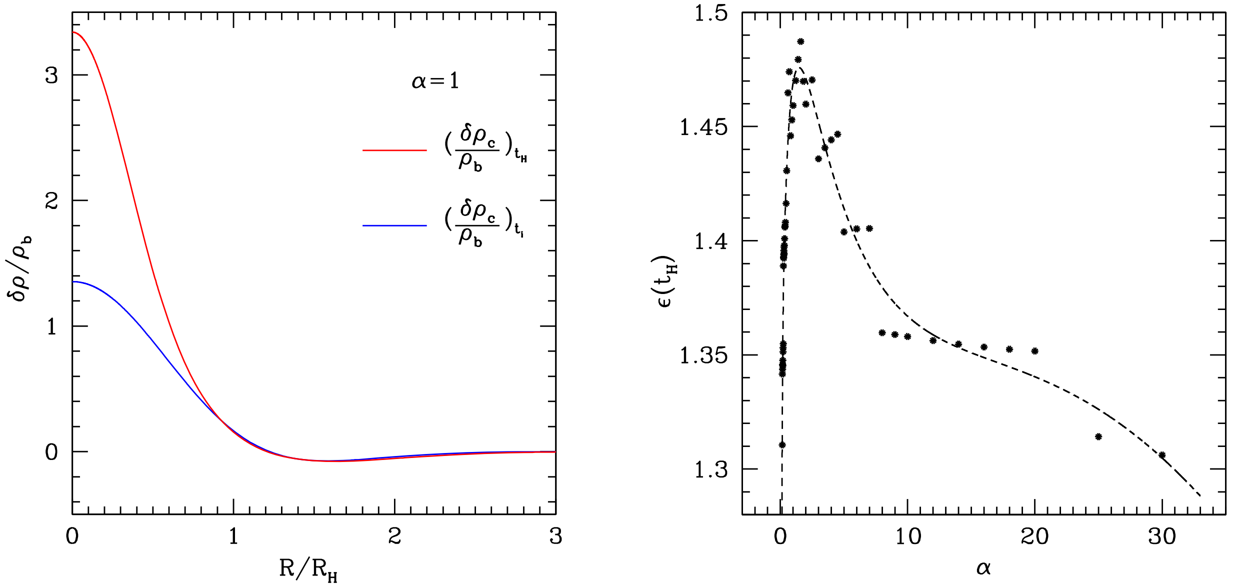

FIG. 5. The left panel shows the critical Mexican-hat profile of the energy density, obtained from (17) with $\alpha = 1$, computed at the horizon crossing, linearly extrapolated ($\epsilon = 1$) with a blue line, and computed numerically at the nonlinear horizon crossing (red line), corresponding in this case to $\epsilon \simeq 1.46$. Both profiles are plotted against R/R_H, where R_H is the radius of the cosmological horizon computed at the corresponding time. The right panel shows how the nonlinear horizon crossing, measured in terms of ϵ, varies when plotted against the shape parameter α, compared to $\epsilon = 1$ at the linear horizon crossing. The dashed line is a polynomial fit of numerical data given by the dots.

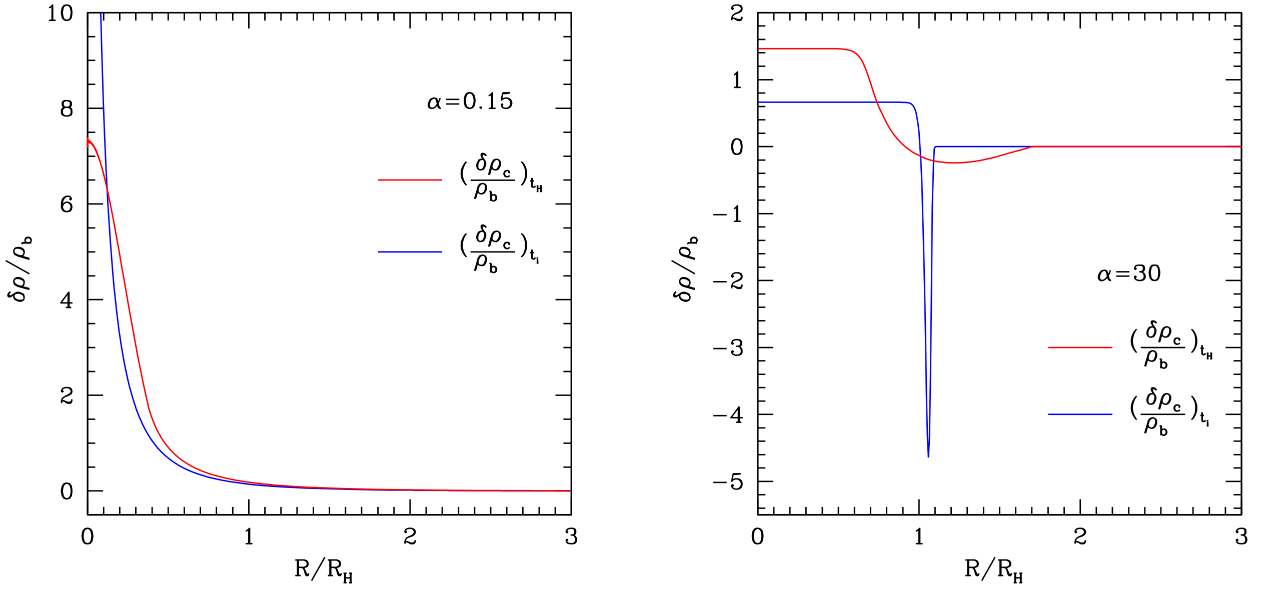

FIG. 6. The two plots of this figure show the critical energy density profiles obtained from (17) with $\alpha = 0.15$ (left panel) and $\alpha = 30$ (right panel), plotted against R/R_H, computed at the horizon crossing linearly extrapolated (blue line) and at the nonlinear one (red line).

For the very sharp profile plotted in the left panel ($\alpha = 0.15$) we can observe instead that the value of the peak amplitude is significantly reduced at the nonlinear horizon crossing with respect the one computed with a linear extrapolation at $\epsilon = 1$. This is because for $\alpha = 0.15$ the profile is not smooth in the center, and there is a significant effect of the local pressure gradients, which are smoothing the profile during the evolution, giving at the nonlinear horizon crossing time a smooth profile with a much lower amplitude of the peak: $\delta\rho_0/\rho_b \simeq 7$ as compared with $\delta\rho_0/\rho_b \simeq 338$ linearly extrapolated at $\epsilon = 1$. A similar effect happens in the under dense region for the top-hat like profile ($\alpha = 30$).

In Figs. 5 and 6 we have analyzed three sample cases of the energy density profiles, seeing how the shape is modified at the nonlinear horizon crossing with respect to the one imposed at initial conditions on super horizon scales, discovering the following general behavior: if the profile is initially smooth, the peak amplitude computed at the nonlinear horizon crossing is higher than the one extrapolated linearly due to nonlinear effects which give an extra growth factor, while when the profile is sharp the behavior is the opposite, due to the nonlinear effects of the pressure gradients smoothing the profile. In general very large values of the peak amplitude at horizon crossing are strongly suppressed because of the smoothing induced by the pressure gradients.

In general the critical amplitude of the peak $\delta\rho_c/\rho_b$ depends on the shape, and in the left panel of Fig. 7 we can see how this quantity is varying with respect to α, for all of the range of shape described by $0.15 \leq \alpha \leq 30$. The linearly extrapolated values of the critical amplitude of the peak, given by (20), are plotted with a blue line, while the values computed at the nonlinear horizon crossing are plotted with a red line.

The linearly extrapolated critical peak values can be computed analytically from (20) while, as shown in the plot, the critical values computed at the nonlinear horizon crossing are given with a good approximation by a simple fit, divided in two regimes.

$$\frac{\delta\rho_c}{\rho_b} \simeq \begin{cases} 10^{0.53-0.17\ln\alpha} & \alpha \lesssim 8 \\ 1.52 & \alpha \gtrsim 8 \end{cases} \tag{43}$$

In the right panel of Fig. 7 we show the ratio between the critical amplitude computed at the nonlinear horizon crossing and the one linearly extrapolated. This shows clearly the two different regimes: the first one, for $\alpha \lesssim 8$, with the critical amplitude varying with α, and the second one for $\alpha \gtrsim 8$ which is almost independent of α, with the peak amplitude converging toward an almost constant value.

The linearly extrapolated value is equal to the one computed numerically for $\alpha \simeq 0.45$, because the energy density profiles obtained from (17) are not smooth if $\alpha \leq 0.5$, with a nonvanishing first derivative in the center. On the contrary, for $\alpha > 0.5$ the energy density profiles are smooth in the center and the perturbation is free to grow without any relevant smoothing of the shape produced by the pressure gradients, reaching a larger value of the critical peak amplitude at the nonlinear horizon crossing with respect to the one linearly extrapolated.

In Fig. 8 the same analysis is made for the threshold δ_c, with the left plot showing the threshold $\delta_c(t_i)$ linearly extrapolated (blue line) and the threshold $\delta_c(t_H)$ computed at the nonlinear horizon crossing (red line). The linearly extrapolated threshold, described with a very good

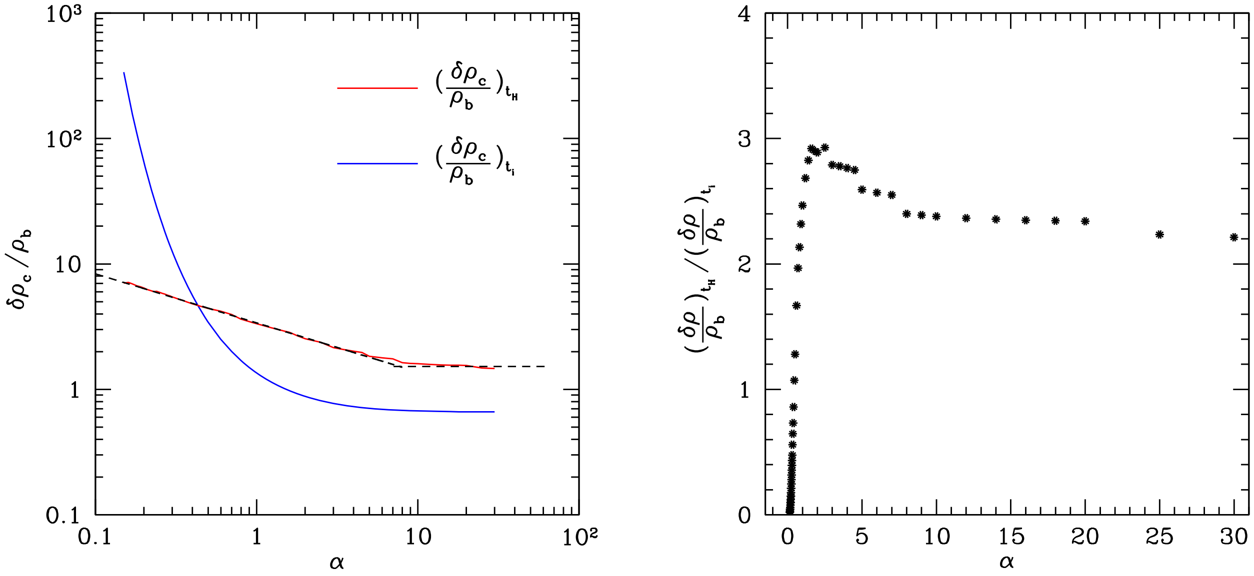

FIG. 7. The left panel of this figure shows the two behaviors of the critical amplitude of the peak $\delta\rho_c/\rho_b$, in one case extrapolated linearly at horizon crossing (blue line) and in the other one computed at the nonlinear horizon crossing (red line), plotted as function of the shape parameter α. The right panel of this figure shows the corresponding ratio of these two quantities.

approximation by the analytic expression of Eq. (19), can be divided into three different regimes, each one described by a simple fit.

$$\delta_c(t_i) \simeq \begin{cases} \alpha^{0.047} - 0.50 & 0.1 \lesssim \alpha \lesssim 7 \\ \alpha^{0.035} - 0.475 & 7 \lesssim \alpha \lesssim 13 \\ \alpha^{0.026} - 0.45 & 13 \lesssim \alpha \lesssim 30 \end{cases} \tag{44}$$

where the first range $0.1 \lesssim \alpha \lesssim 7$ is corresponding with good approximation to all of the shapes of the power spectrum analyzed in Sec. IV, suggesting that the other two ranges are suppressed by the smoothing. They describes energy density profiles which are very sharp around $\hat{r}_m$ where the threshold is computed, and therefore such profiles are smoothed by the pressure gradients, as we have seen in the right panel of Fig. 6, suppressing the values $\delta_c \gtrsim 0.6$.

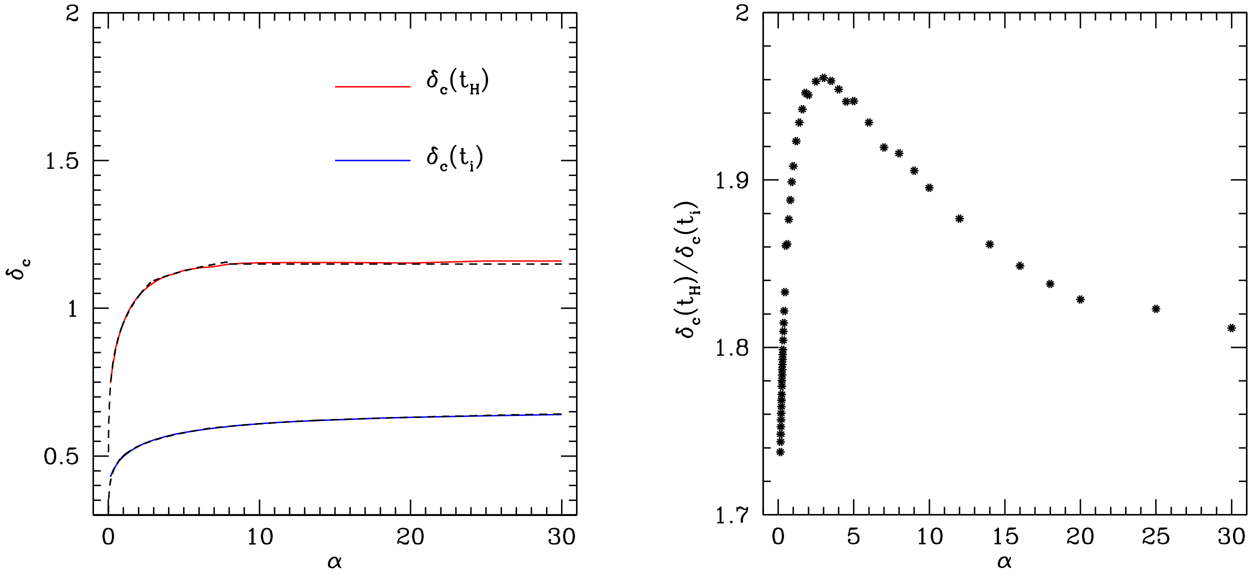

FIG. 8. The left panel of this figure shows the two behaviors of the threshold δ_c in one case extrapolated linearly at horizon crossing (blue line) and in the other one computed at the nonlinear horizon crossing (red line), plotted as a function of the shape parameter α. The right panel of this figure shows the corresponding ratio of these two quantities.

This interpretation is enforced when the threshold is computed at the nonlinear horizon crossing, which is well described by another fit, again divided into three different regimes.

$$\delta_c(t_H) \simeq \begin{cases} \alpha^{0.125} - 0.05 & 0.1 \lesssim \alpha \lesssim 3 \\ \alpha^{0.06} + 0.025 & 3 \lesssim \alpha \lesssim 8 \\ 1.15 & \alpha \gtrsim 8. \end{cases} \tag{45}$$

Here the first regime of (44) is basically splitting into two different behaviors of the threshold computed at the nonlinear horizon crossing time, while the second and the third regimes of (44), corresponding to $\delta_c \gtrsim 0.6$ computed at superhorizon scales, saturate to an almost constant value of the threshold when is computed at t_H.

The right panel of Fig. 8 shows that the ratio between $\delta_c(t_H)$ and $\delta_c(t_i)$, where one can distinguish two different regimes: the first one, when $\alpha \lesssim 3$, is corresponding to the increasing behavior of this ratio, and explains the first regime of (45). The second regime, when $\alpha \gtrsim 3$, has a decreasing behavior of the ratio between the two thresholds, corresponding to the second and third regime of (45), which can be distinguished in the right panel of Fig. 7.

The lower ($\alpha \gtrsim 0.1$) and the upper ($\alpha \lesssim 30$) boundaries of validity of the fit are given by the numerical simulations that are not able to handle very extreme shapes beyond these values. We are however neglecting only a range of α which is not significant as we are already close enough to the limits of δ_c.

Finally we can observe that the difference between the threshold computed at the nonlinear horizon crossing and the linearly extrapolated one is an almost constant numerical coefficient, varying between 1.7 and 2. This underlines the fact that the threshold δ_c is a much more stable quantity than the local critical amplitude of the peak, and has to be preferred for distinguishing between cosmological perturbations forming PBHs and the ones that are bouncing back into the expanding medium.

VI. CONCLUSIONS

PBHs could have formed in the early universe from the collapse of cosmological perturbations at the horizon reentry, provided that their amplitude is larger than a certain critical threshold. In this paper we have provided a simple analytical prescription, summarized in Fig. 9, to compute the threshold of collapse for PBHs, embedding results coming from numerical simulations.

From Gaussian curvature perturbations, one can compute the mean profile on superhorizon scales using peak theory and find the characteristic comoving scale of the perturbations from the given shape of the curvature power spectrum. From the computation of the profile shape parameter on superhorizon scales, one can determine the value of the threshold, also taking into account the effects of nonlinearities arising at the cosmological horizon crossing fitted from numerical simulations. In particular we stress that the thresholds calculated at horizon crossing differs by a factor of order two from the values traditionally adopted in the literature.

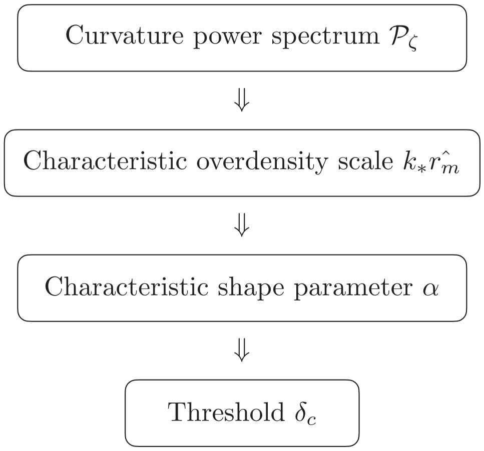

FIG. 9. This diagram summarizes our prescription for computing the threshold δ_c starting from the power spectrum of cosmological curvature perturbations $\mathcal{P}_\zeta$.

By analysing different explicit examples of the curvature power spectrum, we have seen that in general the value of the threshold δ_c is larger for a monochromatic power spectrum, modeled by a Dirac delta, than for a broader shape which allows more modes to contribute to the collapse. The latter gives a broader and flatter profile of the compaction function describing a cosmological perturbation collapsing to form a PBH, corresponding to a lower value of δ_c. This allows us, using (44), to compute the threshold of PBHs measured on super-horizon scales by correctly identifying the shape parameter for a given curvature power spectrum, obtaining $0.4 \lesssim \delta_c \lesssim 0.6$.

However, if the threshold is computed at the nonlinear horizon crossing time (i.e., around the time when they are really formed), the physical range of the threshold δ_c obtained from (45) for all of the possible shapes of the power spectrum is $0.7 \lesssim \delta_c(t_H) \lesssim 1.15$. This might introduce a sizeable contribution in the calculation of the corresponding abundance of PBHs which is exponentially sensitive to the squared value of the threshold $\nu_c \equiv \delta_c/\sigma$, where σ is the variance of the density field of cosmological perturbations. So far in the literature those have been computed on super horizon scales, which gives only the leading order computation of the abundance. Nonlinear effects, becoming important close to the horizon crossing, can give rise to corrections to the probability of collapse estimated on super horizon scale. The full computation of the abundance, however, would require knowing both δ_c and σ at the nonlinear horizon crossing. In this work we have provided the first step in this direction by computing the threshold also at the exact horizon crossing time. The corresponding computation of the variance would however require a dedicated analysis of the nonlinear transfer function, which is beyond the aim of this work.

ACKNOWLEDGMENTS

We thank Silvio Bonometto, Cristiano Germani, John Miller and Sam Young for useful comments. I. M. is supported by the "María de Maeztu" Units of Excellence program MDM-2016-0692 and the Spanish Research State Agency. I. M. thanks the Department of Theoretical Physics of the University of Geneva for financial support and hospitality, and CERN for financial support and hospitality during the final completion of this paper. V.DL., G. F. and A. R. are supported by the Swiss National Science Foundation (SNSF), project *The Non-Gaussian Universe and Cosmological Symmetries*, Project No. 200020-178787.

---

[1] Ya. B. Zel'dovich and I. D. Novikov, Astron. Zh. **43**, 758 (1966) [Sov. Astron. **10**, 602 (1967)].
[2] S. W. Hawking, Mon. Not. R. Astron. Soc. **152**, 75 (1971).
[3] B. J. Carr and S. W. Hawking, Mon. Not. R. Astron. Soc. **168**, 399 (1974).
[4] M. Sasaki, T. Suyama, T. Tanaka, and S. Yokoyama, Classical Quantum Gravity **35**, 063001 (2018).
[5] A. M. Green and B. J. Kavanagh, arXiv:2007.10722.
[6] B. Carr, K. Kohri, Y. Sendouda, and J. Yokoyama, arXiv: 2002.12778.
[7] B. P. Abbott *et al.* (LIGO Scientific and Virgo Collaborations), Phys. Rev. X **9**, 031040 (2019).
[8] R. Abbott *et al.* (LIGO Scientific and Virgo Collaborations), arXiv:2004.08342.
[9] R. Abbott *et al.* (LIGO Scientific and Virgo Collaborations), Astrophys. J. **896**, L44 (2020).
[10] R. Abbott *et al.* (LIGO Scientific and Virgo Collaborations), Phys. Rev. Lett. **125**, 101102 (2020).
[11] S. Bird, I. Cholis, J. B. Munoz, Y. Ali-Haïmoud, M. Kamionkowski, E. D. Kovetz, A. Raccanelli, and A. G. Riess, Phys. Rev. Lett. **116**, 201301 (2016).
[12] M. Sasaki, T. Suyama, T. Tanaka, and S. Yokoyama, Phys. Rev. Lett. **117**, 061101 (2016); **121**, 059901(E) (2018).
[13] S. Clesse and J. García-Bellido, Phys. Dark Universe **15**, 142 (2017).
[14] Y. Ali-Haïmoud, E. D. Kovetz, and M. Kamionkowski, Phys. Rev. D **96**, 123523 (2017).
[15] M. Raidal, C. Spethmann, V. Vaskonen, and H. Veermäe, J. Cosmol. Astropart. Phys. 02 (2019) 018.
[16] G. Hütsi, M. Raidal, and H. Veermäe, Phys. Rev. D **100**, 083016 (2019).
[17] V. Vaskonen and H. Veermäe, Phys. Rev. D **101**, 043015 (2020).
[18] A. D. Gow, C. T. Byrnes, A. Hall, and J. A. Peacock, J. Cosmol. Astropart. Phys. 01 (2020) 031.
[19] V. De Luca, G. Franciolini, P. Pani, and A. Riotto, Phys. Rev. D **102**, 043505 (2020).
[20] V. De Luca, G. Franciolini, P. Pani, and A. Riotto, J. Cosmol. Astropart. Phys. 06 (2020) 044.
[21] K. Jedamzik, J. Cosmol. Astropart. Phys. 09 (2020) 022.
[22] K. Jedamzik, Phys. Rev. Lett. **126**, 051302 (2021).
[23] S. Clesse and J. Garcia-Bellido, arXiv:2007.06481.
[24] A. Hall, A. D. Gow, and C. T. Byrnes, Phys. Rev. D **102**, 123524 (2020).
[25] V. De Luca, V. Desjacques, G. Franciolini, P. Pani, and A. Riotto, Phys. Rev. Lett. **126**, 051101 (2021).
[26] V. De Luca, V. Desjacques, G. Franciolini, and A. Riotto, J. Cosmol. Astropart. Phys. 11 (2020) 028.
[27] K. W. K. Wong, G. Franciolini, V. De Luca, V. Baibhav, E. Berti, P. Pani, and A. Riotto, Phys. Rev. D **103**, 023026 (2021).
[28] Z. Arzoumanian *et al.* (NANOGrav Collaboration), Astrophys. J. Lett. **905**, L34 (2020).
[29] V. Vaskonen and H. Veermäe, Phys. Rev. Lett. **126**, 051303 (2021).
[30] V. De Luca, G. Franciolini, and A. Riotto, Phys. Rev. Lett. **126**, 041303 (2021).
[31] K. Kohri and T. Terada, Phys. Lett. B **813**, 136040 (2021).
[32] G. Domènech and S. Pi, arXiv:2010.03976.
[33] S. Sugiyama, V. Takhistov, E. Vitagliano, A. Kusenko, M. Sasaki, and M. Takada, Phys. Lett. B **814**, 136097 (2021).
[34] K. Inomata, M. Kawasaki, K. Mukaida, and T. T. Yanagida, arXiv:2011.01270.
[35] D. K. Nadezhin, I. D. Novikov, and A. G. Polnarev, Sov. Astron. **22**, 129 (1978).
[36] G. V. Bicknell and R. N. Henriksen, Astrophys. J. **232**, 670 (1979).
[37] I. D. Novikov and A. G. Polnarev, Sov. Astron. **24**, 147 (1980).
[38] K. Jedamzik and J. C. Niemeyer, Phys. Rev. D **59**, 124014 (1999).
[39] M. Shibata and M. Sasaki, Phys. Rev. D **60**, 084002 (1999).
[40] I. Hawke and J. M. Stewart, Classical Quantum Gravity **19**, 3687 (2002).
[41] I. Musco, J. C. Miller, and L. Rezzolla, Classical Quantum Gravity **22**, 1405 (2005).
[42] B. J. Carr, Astrophys. J. **201**, 1 (1975).
[43] T. Harada, C. M. Yoo, and K. Kohri, Phys. Rev. D **88**, 084051 (2013); **89**, 029903(E) (2014).
[44] I. Musco, Phys. Rev. D **100**, 123524 (2019).
[45] A. Escrivà, C. Germani, and R. K. Sheth, Phys. Rev. D **101**, 044022 (2020).
[46] M. W. Choptuik, Phys. Rev. Lett. **70**, 9 (1993).
[47] J. C. Niemeyer and K. Jedamzik, Phys. Rev. Lett. **80**, 5481 (1998).
[48] I. Musco, J. C. Miller, and A. G. Polnarev, Classical Quantum Gravity **26**, 235001 (2009).

[49] I. Musco and J. C. Miller, Classical Quantum Gravity **30**, 145009 (2013).

[50] D. H. Lyth, K. A. Malik, and M. Sasaki, J. Cosmol. Astropart. Phys. 05 (2005) 004.

[51] A. G. Polnarev and I. Musco, Classical Quantum Gravity **24**, 1405 (2007).

[52] T. Harada, C. M. Yoo, T. Nakama, and Y. Koga, Phys. Rev. D **91**, 084057 (2015).

[53] J. M. Bardeen, J. R. Bond, N. Kaiser, and A. S. Szalay, Astrophys. J. **304**, 15 (1986).

[54] C. Germani and I. Musco, Phys. Rev. Lett. **122**, 141302 (2019).

[55] C. M. Yoo, T. Harada, J. Garriga, and K. Kohri, Prog. Theor. Exp. Phys. **2018**, 123 (2018).

[56] S. Young, C. T. Byrnes, and M. Sasaki, J. Cosmol. Astropart. Phys. 07 (2014) 045.

[57] C. M. Yoo, T. Harada, S. Hirano, and K. Kohri, arXiv:2008.02425.

[58] M. Kawasaki and H. Nakatsuka, Phys. Rev. D **99**, 123501 (2019).

[59] S. Young, I. Musco, and C. T. Byrnes, J. Cosmol. Astropart. Phys. 11 (2019) 012.

[60] V. De Luca, G. Franciolini, A. Kehagias, M. Peloso, A. Riotto, and C. Ünal, J. Cosmol. Astropart. Phys. 07 (2019) 048.

[61] C. Germani and R. K. Sheth, Phys. Rev. D **101**, 063520 (2020).

[62] S. Young and M. Musso, J. Cosmol. Astropart. Phys. 11 (2020) 022.

[63] S. Young and C. T. Byrnes, J. Cosmol. Astropart. Phys. 08 (2013) 052.

[64] S. Young, D. Regan, and C. T. Byrnes, J. Cosmol. Astropart. Phys. 02 (2016) 029.

[65] G. Franciolini, A. Kehagias, S. Matarrese, and A. Riotto, J. Cosmol. Astropart. Phys. 03 (2018) 016.

[66] C. M. Yoo, J. O. Gong, and S. Yokoyama, J. Cosmol. Astropart. Phys. 09 (2019) 033.

[67] A. Kehagias, I. Musco, and A. Riotto, J. Cosmol. Astropart. Phys. 12 (2019) 029.

[68] A. Kalaja, N. Bellomo, N. Bartolo, D. Bertacca, S. Matarrese, I. Musco, A. Raccanelli, and L. Verde, J. Cosmol. Astropart. Phys. 10 (2019) 031.

[69] K. Tomita, Prog. Theor. Phys. **54**, 730 (1975).

[70] D. S. Salopek and J. R. Bond, Phys. Rev. D **42**, 3936 (1990).

[71] M. Kopp, S. Hofmann, and J. Weller, Phys. Rev. D **83**, 124025 (2011).

[72] S. Young, Int. J. Mod. Phys. D **29**, 2030002 (2020).

[73] A. Moradinezhad Dizgah, G. Franciolini, and A. Riotto, J. Cosmol. Astropart. Phys. 11 (2019) 001.

[74] V. De Luca, G. Franciolini, and A. Riotto, Phys. Lett. B **807**, 135550 (2020).

[75] A. Helou, I. Musco, and J. C. Miller, Classical Quantum Gravity **34**, 135012 (2017).

[76] V. Faraoni, G. F. R. Ellis, J. T. Firouzjaee, A. Helou, and I. Musco, Phys. Rev. D **95**, 024008 (2017).